Research Article Vol. 26, No. 21 | 15 Oct 2018 | OPTICS EXPRESS 27504

Optics EXPRESS

Photon-induced carrier recombination in the nonlayered-structured hybrid organic-inorganic perovskite nano-sheets

Di Wang,[1, 2] **Wen-Bo Shi,**[1] **Hao Jing,**[1] **Chunyang Yin,**[1] **Yingying Zhu,**[1] **Jing Su,**[3] **Guo-Bin Ma,**[1] **Ruwen Peng,**[1,4] **Xiaoyong Wang,**[1] **and Mu Wang**[1,5]

[1] *National Laboratory of Solid State Microstructures, School of Physics, and Collaborative Innovation Center of Advanced Microstructures, Nanjing University, Nanjing 210093, China*
[2] *Institute of Functional Crystals, Tianjin University of Technology, Tianjin 300384, China*
[3] *School of Physics & Optoelectronic Engineering, Nanjing University of Information Science &Technology, Nanjing 210044, China*
[4] *rwpeng@nju.edu.cn*
[5] *muwang@nju.edu.cn*

Abstract: The hybrid organic-inorganic perovskites (HOIPs) have attracted much attention recently due to their preeminent efficiency in solar cells. According to the difference on the crystalline structure, the HOIPs could be classified into layered and non-layered perovskites. Very recently, it has been realized that the non-layered HOIPs with common-vertex structure possess even better opto-electrical performance. Yet the carrier recombination mechanism in perovskite remains not very clear, and a clear understanding of this mechanism is essential to pinpoint the working mechanism of photovoltaic and electroluminescent materials. Here we report the optical studies on the hybrid perovskite crystalline nano-sheet of $CH_3NH_3PbBr_3$ with common-vertex structure. It is shown that the non-layered perovskite crystalline nanosheets possess the exciton binding energy about two orders of magnitude smaller than that of the layered perovskite and the colloidal nanoplates, which is beneficial for the designing of the high-efficiency photovoltaic devices. By measuring the temperature-dependent photoluminescence (PL) spectra, the excitation-power-variant PL spectra, and the time-resolved PL spectra, we identify that both the free-carrier and the localized exciton recombination channels may coexist in the crystallites. Further, for the thin crystallite (~60 nm), the free-carrier recombination channel dominates; whereas when the thickness increases beyond 200 nm, the localized exciton recombination channel plays the major role. We suggest these results are helpful to improve further the photovoltaic and electroluminescent performances of perovskite devices.

1. Introduction

The generation, separation, and transportation of electric charge carriers are the important issues in harvesting solar energy with semiconductor solar cells [1]. The merit of a solar-cell material largely depends on its capability to generate free charge carriers and sustain a high density of charge carriers under continuous illumination. Understanding the mechanisms of these fundamental processes is essential for the designing and optimization of solar cell materials. Recently hybrid organic-inorganic perovskites (HOIPs) have attracted much attention and become a promising photovoltaic (PV) material [2]. HOIPs possess superior optical and electronic properties, such as the strong absorption for visible light, the efficient carrier transportation with a long diffusion length, tunable bandgap and relatively low defect density, etc [3–10]. More importantly, this material can be fabricated by low-cost wet chemistry processes, and exhibit excellent performance similar to that of single crystalline

#342142 https://doi.org/10.1364/OE.26.027504
Journal © 2018 Received 13 Aug 2018; revised 25 Sep 2018; accepted 26 Sep 2018; published 5 Oct 2018

GaAs [11]. Recently the solar cell fabricated with HOIPs as PV active material has achieved a certified power conversion efficiency (PCE) of 25.2% [12]. Thin sheets of HOIPs without the layered structure are very attractive because of their much smaller binding energy than that of the layered perovskite and colloidal nanoplates [13–17]. The smaller binding energy helps to improve the power conversion efficiency of HOIPs-based photovoltaic. On the other hand, there are quite a few debatable issues for these materials, such as the verifying the type of photo-induced carrier, the exciton properties, and the impact of crystalline morphologies on carriers, etc.. Clarifying these issues will certainly boost the development of HOIPs-based solar cells.

The absorption spectroscopy and photoluminescence (PL) spectroscopy are known to be the efficient tools to investigate the ways of photo-induced carrier recombination. The binding energy of exciton in perovskites can be determined from the band-edge absorption spectra [18,19]. It has been suggested that photo-inducted electron-hole pairs prefer to be separated, and the role of bound excitons can be neglected due to thermal dissociation at room temperature. In contrast, power-dependent PL spectra suggest that the carrier dynamics in the solution-grown perovskite films is dominated by localized excitons [20], which are very common due to widely existing crystal defects in the material. Yet up to now, it remains unclear whether photon absorption can induce the direct formation of free-carriers or excitons. In addition, it has been observed that the fabrication conditions of a perovskite film determine its microstructure [23], hence affect its bandgap, carrier type, and recombination channel, etc [24]. These parameters affect the device performance [25]. We expect that the mechanism of photo-induced carrier recombination is an important issue both in designing materials for photovoltaic and in light-emitting applications [26].

In this work, we take the solution-grown single-crystalline $MAPbBr_3$ nano-sheet as an example, determine the exciton binding energy (E_B), which is the fundamental parameter in understanding the working mechanism of HOIPs-based photovoltaic devices. Then we explore the photo-induced carrier mechanism by temperature-dependent and excitation-power-variant PL spectra. We demonstrate that both the free-carrier recombination and the localized exciton recombination channels coexist inthe HOIPs. When the crystallite is very thin (60 nm), the free-carrier recombination channel dominates; whereas when the thickness increases (>200 nm), the localized exciton recombination channel becomes much more important.

2. Grow $MAPbBr_3$ single-crystalline nano-sheets on mica substrate

Ultrathin $MAPbBr_3$ crystallite sheets are grown in a thin layer of solution film spin-coated on a freshly cleaved mica surface. The $MAPbBr_3$ solution is synthesized by dissolving $MAPbBr_3$ powder in hydrobromic acid (HBr, 48wt.%) and N,N-Dimethylformamide (DMF, 57wt.%), respectively. Nucleation and growth of $MAPbBr_3$ are carried out inside an argon-filled glove box. By controlling the evaporation rate of solvent with the temperature, square crystalline sheets of $MAPbBr_3$ with different thicknesses can be nucleated and grown on the mica substrate.

Figure 1(a) shows the optical micrograph of the as-grown ultrathin $MAPbBr_3$ crystalline sheets (the bright squares) on the mica substrate. The bright field and fluorescence images of the grown $MAPbBr_3$ sheets are observed by Nikon optical microscope (ECLIPSE 80i). The lateral size of the crystalline sheets can reach about 10 μm. The sheet thickness can be qualitatively distinguished by its color with optical microscopy, where the thinner sheets appear lighter (colorless or gray), and the thicker crystalline sheets possess different color due to optical interference. The thickness and surface morphology of $MAPbBr_3$ are measured by an atom force microscope (AFM; Digital Instruments MultimodeTM SPM) in tapping mode. When the sheet becomes thicker than 200 nm (the refractive index of $MAPbBr_3$ is around 2.0 in visible regime [27]), the color of the crystalline sheet does not change anymore, instead, it shows an intrinsic orange color which is determined by the bandgap of $MAPbBr_3$. Figure 1(b) illustrates the fluorescent micrographs of the as-grown sheets corresponding to that in Fig. 1(a). The $MAPbBr_3$ sheets exhibit strong green fluorescent emission, and the luminescence along the edges of the sheets is much stronger than that in the inner parts.

The $MAPbBr_3$ perovskite crystal has a cubic symmetry with space group Pm-3m (Z = 1) at room temperature [28]. As illustrated in Fig. 1(c), the metal-halogen octahedral $[PbBr_6]^-$ locates at eight corners of the cubic. The organic cations MA^+ locate at the interstice of the $[PbBr_6]^-$ octahedral cages. In such common-vertex-structured $MAPbBr_3$ perovskite crystal, as illustrated in Fig. 1(c), the upper layer is $PbBr_6$ octahedral structure, the lower layer is also $PbBr_6$ octahedral structure. These two layers are connected by sharing Br atoms. This structure is different from the layered perovskite crystal, such as $(C_4H_9NH_3)_2PbBr_4$ [29], where the different layers are connected by van de Waals bonding.

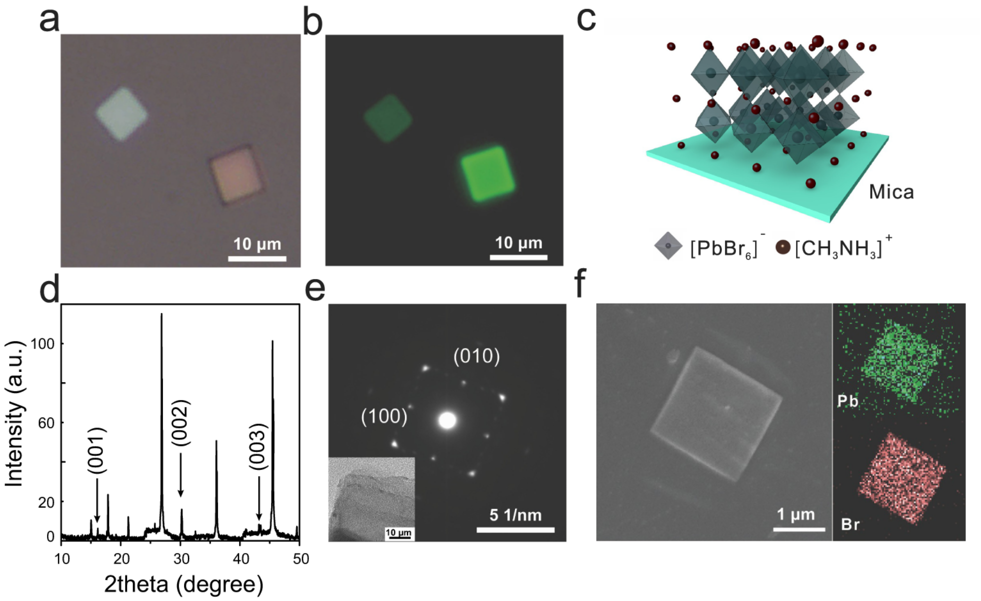

Fig. 1. (a) The optical micrograph of the as-grown $MAPbBr_3$ sheets on a mica substrate. (b) Green luminescence of the as-grown $MAPbBr_3$ sheets observed in fluorescence microscopy. (c) Structure of a single cell $MAPbBr_3$ crystal (the gray octahedra stand for $[PbBr_6]^-$; the dark red balls stand for $[CH_3NH_3]^+$ ions). (d) The XRD spectrum of the as-grown 2D $MAPbBr_3$ sheet. (e) The electron diffraction pattern and TEM micrograph of the $MAPbBr_3$ sheet. (f) SEM micrograph of an ultrathin $MAPbBr_3$ and EDS mapping of element distributions for lead and bromine, respectively.

X-ray diffraction (XRD) and transmission electron microscopy ((TEM; JEOL JEM-1011)) are applied to determine the crystalline phase of the as-grown $MAPbBr_3$ sheets and selected-area electron diffraction (SAED) indicates that the crystallite grows in [100] direction (Fig. 1(e)). Additional peaks in XRD spectrum (Fig. 1(d)) come from the mica substrate, which agree with the previous report [30]. TEM samples have been prepared by using lacey carbon Cu grid to scratch the surface of the mica substrate, and SEM samples have been prepared by coating a thin layer of carbon. Analysis of the diffraction pattern (Fig. 1(e)) shows that the lattice constant is a = 6.043 Å. In addition, the energy dispersive spectroscopy (EDS) mapping illustrates that the distribution of elements Pb and Br is homogeneous across the crystallite (Fig. 1(f)).

3. The exciton binding energy obtained from both absorption spectra and temperature-dependent PL spectra

Figures 2(a)-2(c) illustrate the typical absorption spectra and the photoluminescence (PL) spectra of a 65.4 nm-thick $MAPbBr_3$ crystalline sheet at room temperature. The optical absorptions carried out with a micro-spectrophotometer (CRAIC, 20/30 PV Tm). The PL spectra are collected by a confocal micro-Raman system (Princeton Instrument). Unlike the sharp step of optical absorption of a bulk $MAPbBr_3$ crystal [31], here a bump appears at the absorption edge of the sheet. This feature indicates that the optical absorption of $MAPbBr_3$ sheet consists of two components: the continuum absorption and the peak absorption, and the latter will be proven as the exciton absorption. While the PL spectrum exhibits an asymmetric feature, which can be disassociated to Peak 1 (centered at 532 nm) and Peak 2 (centered at 545 nm) by two-Gaussian-function fitting.

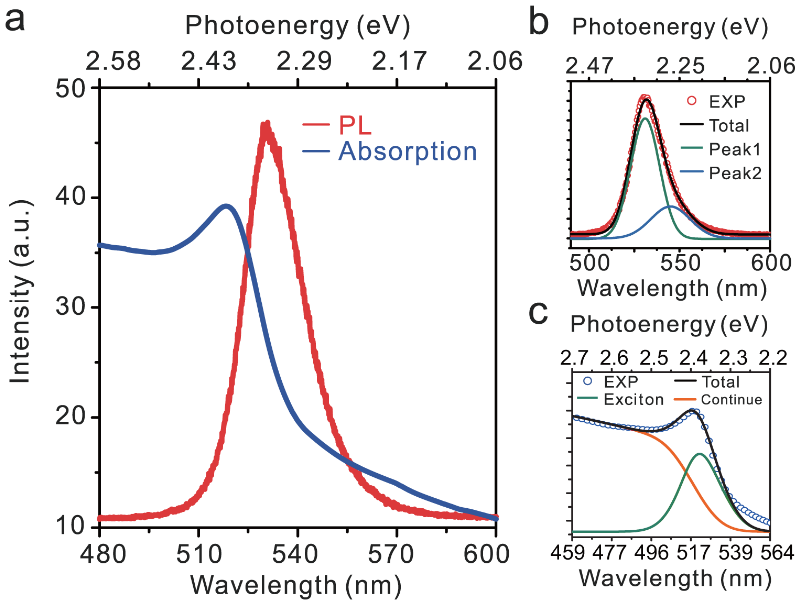

Fig. 2. (a) Steady-state absorption (blue line) and photoluminescence (red line) spectra of an 2D $MAPbBr_3$ sheet (thickness 65.4 nm) at room temperature. The PL spectrum is excited by a continuous wave laser (450 nm). (b) The PL spectrum can be de-convoluted into two-Gaussian profile functions, the free-carrier recombination peak (green solid line) and exciton recombination peak (blue solid line). (c) The theoretical absorption coefficient (black solid line) is calculated based on Elliott's formula, which includes the excitonic (green solid line) and free-carrier continuum (red solid line) components. In both b and c, the experimental data (open circles) and the calculated ones (solid lines) are in good agreement.

The absorption coefficient $\alpha(\hbar\omega)$ of a 2D $MAPbBr_3$ sheet, which is associated with continuum absorption and exciton absorption, can be described by the Elliott model involving bandgap E_g (the continuum part) and exciton binding energy E_B (the exciton part) [16,32] as

$$\alpha(\hbar\omega) \propto \frac{\mu_{CV}^2}{\hbar\omega}\sqrt{E_B}\left[\sum_n \frac{4\pi E_B}{n^3}\delta(\hbar\omega - E_n^B) + \frac{2\pi\sqrt{E_B}\,\theta(\hbar\omega - E_g)}{1 - e^{-2\pi\sqrt{E_B/(\hbar\omega - E_g)}}}\right] \qquad (1)$$

Here μ_{CV}^2 is the squared transition dipole moment, E_g is the bandgap, E_B is the exciton binding energy, E_n^B is the energy of nth state. The first term in Eq. (1), the delta function $\delta(\hbar\omega - E_n^B)$, represents the excitonic transition to the nth state with energy $E_n^B = E_g - E_B / n^2$; the second term is a Heaviside step function $\theta(\hbar\omega - E_g)$, which represents the continuum band-to-band transition above bandgap E_g. To describe the line broadening and the non-parabolic dispersion of energy band in experiments, a Gaussian function is convoluted with the delta function and the Heaviside step function, respectively, and the line width is represented by Γ [33]. At room temperature, excitons are hard to be spectrally resolved for $n > 1$. So, in this work we assume $n = 1$ for the exciton transition. Based on the absorption data (Fig. 2(a)), we obtain the bandgap E_g as 2.41 ± 0.01 eV and the exciton binding energy E_B as 16 ± 3.4 meV in the $MAPbBr_3$ crystalline sheet with thickness around 60 nm, respectively.

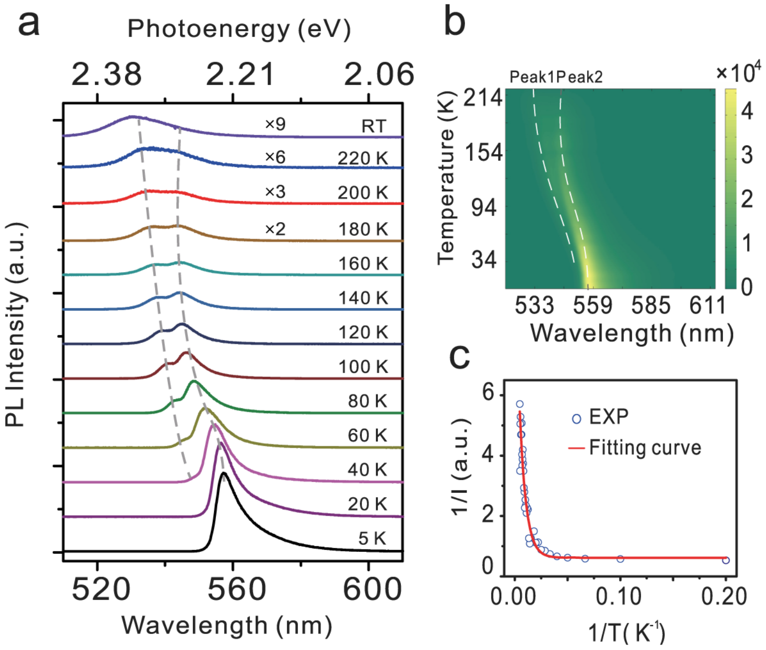

Fig. 3. (a) The temperature-dependent PL spectra of $MAPbBr_3$ sheets. By decreasing temperature, the 545 nm peak (Peak2) enhances gradually and red-shift; in contrast, the 532 nm peak (Peak1) decays. (b) The temperature-dependent PL mapping of the 2D $MAPbBr_3$ sheet. (c) Temperature dependence of the intensities of Peak2. By fitting the experiment data, we estimate E_B as 14 meV.

To identify the origin of the absorption peak in $MAPbBr_3$ crystal nano-sheets, we carry out temperature-dependent PL measurements (Figs. 3(a)-3(c)). For temperature-dependent PL measurements, the perovskite samples are mounted in a liquid helium cryostat (Janis ST-500-UC) in vacuum (10^{-5}Torr) and the temperature can be tuned from 220 K to 5 K (Cryogenic Control System, Inc. model 22C). By decreasing temperature from 220K to 5K, the intensity of Peak 1 decreases continuously. It is known that at low temperature thermal phonons are frozen, and the dissociation of exciton to free carriers is suppressed. Then the intensity of free carriers is reduced [34,35]. Consequently, we can infer that the Peak 1 is contributed by the recombination of free carriers. In contrast, the Peak 2 gradually increases in intensity and red-shifts. Such a feature meets the typical characteristics of localized excitons [36]. At lower temperature, more thermal phonons are frozen, so the intensity of exciton emission is enhanced. The thermodynamic equilibrium between excitons and free carriers depends on the binding energy of exciton (E_B). Therefore, we can attribute the increase of the intensity of the Peak 2 to the exciton recombination. The temperature-dependent PL intensity contributed by the excitons can be described as [37,38]:

$$I_e(T) = \frac{I_0}{1 + Ae^{-E_B/k_BT}}, \tag{2}$$

where I_0 is the PL intensity at zero temperature, and k_B is the Boltzmann constant. From the integration strength of the PL spectra at different temperatures (Fig. 3(c)), we obtain E_B as around 14 meV. Obviously, the binding energy of excitons retrieved from the absorption spectrum is in good agreement with that from the temperature-dependentPL spectra shown here.

4. Two different carrier recombination channels

To elucidate further the photo-induced recombination process in the $MAPbBr_3$nano-sheet, we measure the PL spectra at different excitation power. As an example, Figs. 4(a) and 4(c) show the excitation-power-variant PL spectra of a 65.4 nm-thick sample at room temperature and 100K, respectively. The excitation power of the incident light varies from 50 to 400 mW. Each PL spectrum can be deconvoluted into two peaks centered around 532 nm and 545 nm, respectively. The integrated PL intensity I_{PL} of each peak can be fitted by the power-law relation with respect to the excitation intensity I_{ex} as $I_{PL} \propto I_{ex}^k$. According to the carrier recombination model [39,40], $k = 2$ corresponds to the free-carrier recombination, and $1<k<2$ corresponds to the exciton recombination (including free excitons and localized excitons). At room temperature, $k = 2.0$ for the peak at 532 nm and $k = 1.8$ for the peakat 545 nm; while at the temperature of 100K, $k = 2.1$ for the peak at 532 nm and $k = 1.5$ for the peak at 545 nm. All these suggest that the peak at 532 nm is contributed by the free-carrier recombination, whereas the peak at 545 nm is associated with the localized exciton recombination.

The time-resolved photoluminescence (TRPL) investigation further proves different carrier recombination of PL emissions. The excitation source for the time-resolved photoluminescence measurement is a picosecond diode laser (P-C-405B, Picoquant) (output wavelength 405 nm) with a repetition rate of 5 MHz. As shown in Fig. 4(e), the data of the decay time can be fitted by multi-exponential function [41]:

$$I(t) = \sum_{i=1}^{M} A_i \exp(-\mathrm{t}/\tau_i), \tag{3}$$

where A_i and τ_i are the amplitudes and lifetimes of the ith exponential components of the fluorescence. In this work, the lifetime of fluorescence in the perovskite sheet is fitted with bi-exponential function. It is found that the lifetime of photo-induced carriers in $MAPbBr_3$ sheet at two peaks contains both fast (τ_1) and slow (τ_2) components. For the wavelength 532 nm, $\tau_1 = 3.0$ ns, $\tau_2 = 9.4$ ns, the weight ratio of the two components is R = 67%: 33%; for the wavelength 545 nm, $\tau_1 = 3.8$ ns, $\tau_2 = 11.1$ ns, and the weight ratio of the two components is R = 60%: 40% (the fitting residuals of the two peaks are smaller than 2%). One may find that at wavelength 532 nm, the fast component has higher percentage; at wavelength 545 nm, the percentage of the fast component drops and the percentage of the slow component increases. The fast and slow components may be related to the free carrier recombination and localized exciton recombination, respectively. Physically, the photo-generated carries occupy the extended states firstly, part of these carries recombine quickly to be the fast components in TRPL, while other carries relax to the localized states because of the common existed tail states in solution-processed perovskites [20]. After that, excitons in the band of localized statesare subject to a much slower redistribution [42,43] and the recombination of these localized excitons will be contributed to the slow components of the TRPL. Besides, some other factors may also influence the fast and slow components. For example, owing to the existence of the trap states, the carrier-trapping decay may contribute to the fast component [44], while the two-carrier recombination process may relate to the slow component [45].

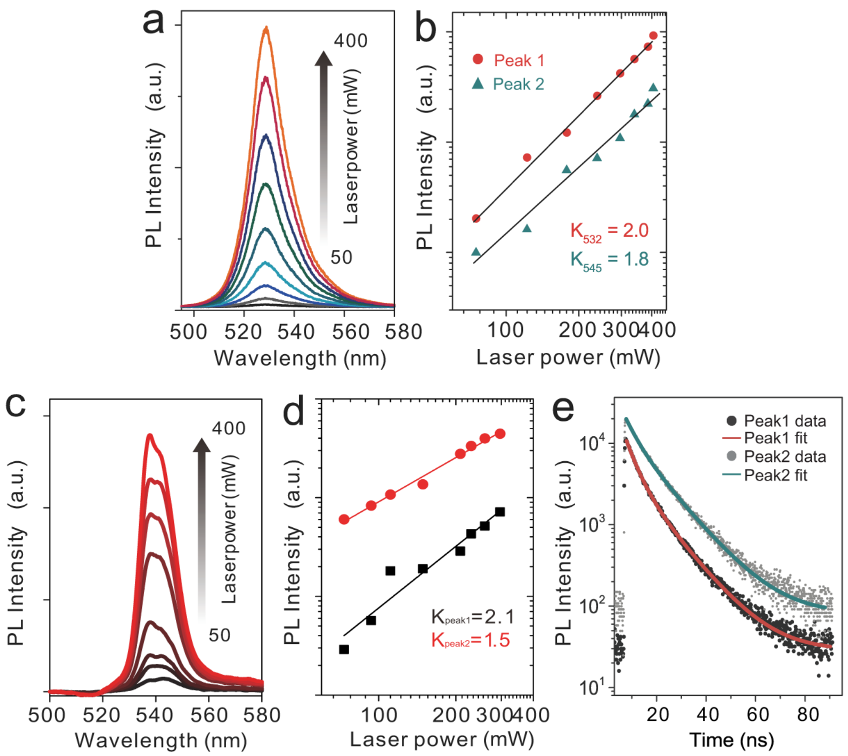

Fig. 4. (a)Power-dependent PL spectra at room temperature for a crystallite 65.4 nm in thickness. (b) The logarithm plot of the integrated intensity of the photoluminescence peaks at 532 and 545 nm, respectively, as a function of the excitation power. (c) Power-dependent PL spectra at 100K for a crystallite 60.7 nm in thickness. (d) The logarithm plot of the integrated PL intensity for (c). (e) The decay-time spectra of 532 nm (Peak1) and 545 nm (Peak2) at room temperature, respectively.

We also measure the PL spectra of $MAPbBr_3$ crystallites with different thicknesses as shown in Fig. 5(a). When the crystallite thickness is thinner than 60 nm, meanwhile the dominant peak appears at 532 nm (denoted as Peak 1). As the crystallite thickness increases, an additional peak appears at 545 nm (denoted as Peak 2) in addition to the original Peak 1. When the thickness increases beyond 200 nm (227 nm in Fig. 5a), Peak 2 dominates. When the crystallite sheet thickness is in between 60 nm and 200 nm, both Peak 1 and Peak 2 are important. As shown in Fig. 5(b), it is reasonable to suggest that when the excitation light (λ_0) incidents on the surface of a $MAPbBr_3$ sheet, electrons transit from the valence band (VB) to the conduction band (CB), and then rapidly relax to the bottom of the CB as the free carriers. Part of the free electrons may combine with the holes to form localized excitons [46–48]. Consequently, the excitons possess slightly lower energy than that of the free carries. Meanwhile, the recombination of photo-induced carriers in a $MAPbBr_3$ sheet may have the following two routes: recombination of free carriers and recombination of localized excitons. These two routes are associated with the optical radiations with wavelength of λ_1 and λ_2, respectively. For example, for the 65.4 nm-thick $MAPbBr_3$crystallite, the detected PL spectrum can be deconvoluted into two peaks centered at 532 nm (λ_1, Peak 1) and 545 nm (λ_2, Peak 2) (although Peak 1 is much more dominant than Peak 2), as shown in Fig. 2b. It should be mentioned that similar phenomenon has been observed in the bulk single-crystal $MAPbBr_3$, *i.e.*, multiple fluorescence peaks have been observed, which come from multiple intrinsic exciton states in the bulk perovskite [21,22]. But in our case, the perovskite sheet is thin enough, the two emission peaks originate from the radiative recombination due to excitons and free carriers, respectively.

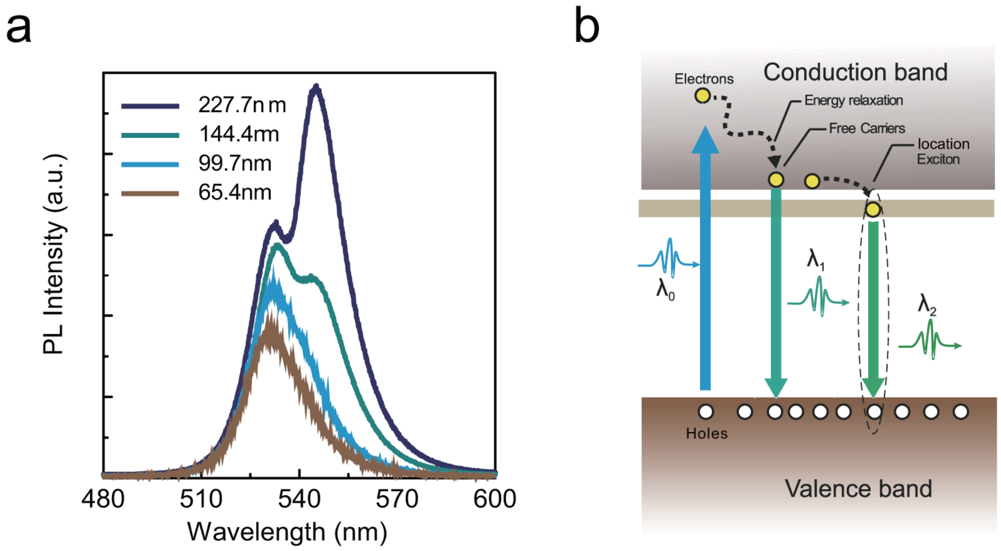

Fig. 5. (a) Steady-state PL spectra of ultrathin $MAPbBr_3$ sheets with different thickness. (b) Schematics to show different carrier recombination channels in a$MAPbBr_3$ sheet based on PL studies. The yellow dots in the conduction band and the whitedots in the valence band respectively represent electrons and holes created by the absorption ofexcitation light. The excited electrons rapidly release to the bottom of conduction band and return to the ground state via two radiative recombination channels: the free-carrier channel (λ_1), and the exciton channel (λ_2).

In order to understand the effect that the channel changes with the thickness of the nano-sheets, we emphasis the two physical processes, *i.e.*, exciton dissociations and self-absorption in the perovskite. The former involves in the photo-induced exciton dissociation owing to the edge state and the surface state of perovskites [49]. The latter is that the luminescence of perovskite could be reabsorbed by itself [50,51]. When the sheet is thin enough, the edge and surface states in perovskites could not be neglected. The photo-induced excitons will be dissociated by the edge and surface states, which means that the exciton recombination at 545 nm is suppressed in thin perovskite. With the thickness increasing, optical guiding effect appears in the perovskite. The illumination light passes through the perovskite and is resorbed by itself. In this case, the 532 nm emission attributed to the free carriers is resorbed in perovskite, and it transfers the energy to the lower state of localized excitons. Consequently, the 545 nm emission coming from the exciton recombination is enhanced due to the self-absorption effect. Actually, these processes may cause the changes in the recombination channels.

5. Conclusion

To summarize, we report in this work the studies on $MAPbBr_3$ crystalline nano-sheets prepared by spin-coating solution growth. Electron diffraction indicates that the $MAPbBr_3$ crystallites possess non-layered structure. Two types of carrier recombination channels, *i.e.*, free carrier recombination and localized exciton recombination, have been identified by temperature-dependent PL spectra and excitation-power-variant PL spectra.When the crystalline sheet is very thin (~60 nm), free-carrier recombination channel dominates; whereas when the thickness increases (> 200 nm), localized exciton recombination channel plays the major role. The exciton binding energy of $MAPbBr_3$ nano-sheets is obtained via optical absorption spectra and temperature-dependent PL spectra, which is of the order of 10 meV, two orders of magnitude smaller than that of layered perovskites and colloidal nanoplates. It has been well established that with lower exciton binding energy, the excitons can be dissociated to free carriers more easily. Thus, we expect that the dominance of free carriers in $MAPbBr_3$ sheet is beneficial for high-efficiency photovoltaic devices. We also expect that the mechanism of photo-induced carrier recombination in HOIPs nano-sheet is highly intuitive for future high-performance optoelectronic applications.

Funding

National Key R&D Program of China (2017YFA0303702); the National Natural Science Foundation of China (11474157, 11634005, 51472123, 11674155, 61475070, 51302268, 11621091); and partially by the "333 Project" from Jiangsu Province (BRA2016350).

Acknowledgments

D. W. and W.-B. S. contributed equally to this work.

References

1. L. F. Alan and H. B. Richard, *Fundamental of Solar Cell: Photovoltaic Solar Energy Conversion*, (Academic, 1983).
2. W. Zhang, G. E. Eperon, and H. J. Snaith, "Metal halide perovskites for energy applications," Nat. Energy **1**(6), 16048 (2016).
3. A. Kojima, K. Teshima, Y. Shirai, and T. Miyasaka, "Organometal halide perovskites as visible-light sensitizers for photovoltaic cells," J. Am. Chem. Soc. **131**(17), 6050–6051 (2009).
4. D. Shi, V. Adinolfi, R. Comin, M. Yuan, E. Alarousu, A. Buin, Y. Chen, S. Hoogland, A. Rothenberger, K. Katsiev, Y. Losovyj, X. Zhang, P. A. Dowben, O. F. Mohammed, E. H. Sargent, and O. M. Bakr, "Solar cells. Low trap-state density and long carrier diffusion in organolead trihalide perovskite single crystals," Science **347**(6221), 519–522 (2015).
5. G. Xing, N. Mathews, S. S. Lim, N. Yantara, X. Liu, D. Sabba, M. Grätzel, S. Mhaisalkar, and T. C. Sum, "Low-temperature solution-processed wavelength-tunable perovskites for lasing," Nat. Mater. **13**(5), 476–480 (2014).
6. W. J. Yin, T. Shi, and Y. Yan, "Unusual defect physics in CH3NH3PbI3 perovskite solar cell absorber," Appl. Phys. Lett. **104**(6), 063903 (2014).
7. J. C. Blancon, H. Tsai, W. Nie, C. C. Stoumpos, L. Pedesseau, C. Katan, M. Kepenekian, C. M. M. Soe, K. Appavoo, M. Y. Sfeir, S. Tretiak, P. M. Ajayan, M. G. Kanatzidis, J. Even, J. J. Crochet, and A. D. Mohite, "Extremely efficient internal exciton dissociation through edge states in layered 2D perovskites," Science **355**(6331), 1288–1292 (2017).
8. B. Du, W. Yang, Q. Jiang, H. Shan, D. Luo, B. Li, W. Tang, F. Lin, B. Shen, Q. Gong, X. Zhu, R. Zhu, and Z. Fang, "Plasmonic-Functionalized Broadband Perovskite Photodetector," Adv. Opt. Mater. **6**(8), 1701271 (2018).
9. Y. Song, C. Zhang, W. Liu, X. Li, H. Long, K. Wang, B. Wang, and P. Lu, "High-efficiency energy transfer in perovskite heterostructures," Opt. Express **26**(14), 18448–18456 (2018).
10. J. Xing, Y. Zhao, M. Askerka, L. N. Quan, X. Gong, W. Zhao, J. Zhao, H. Tan, G. Long, L. Gao, Z. Yang, O. Voznyy, J. Tang, Z. H. Lu, Q. Xiong, and E. H. Sargent, "Color-stable highly luminescent sky-blue perovskite light-emitting diodes," Nat. Commun. **9**(1), 3541 (2018).
11. A. Polman, M. Knight, E. C. Garnett, B. Ehrler, and W. C. Sinke, "Photovoltaic materials: Present efficiencies and future challenges," Science **352**(6283), aad4424 (2016).
12. F. Sahli, J. Werner, B. A. Kamino, M. Bräuninger, R. Monnard, B. Paviet-Salomon, L. Barraud, L. Ding, J. J. Diaz Leon, D. Sacchetto, G. Cattaneo, M. Despeisse, M. Boccard, S. Nicolay, Q. Jeangros, B. Niesen, and C. Ballif, "Fully textured monolithic perovskite/silicon tandem solar cells with 25.2% power conversion efficiency," Nat. Mater. **17**(9), 820–826 (2018).
13. O. Yaffe, A. Chernikov, Z. M. Norman, Y. Zhong, A. Velauthapillai, A. van der Zande, J. S. Owen, and T. F. Heinz, "Excitons in ultrathin organic-inorganic perovskite crystals," Phys. Rev. B Condens. Matter Mater. Phys. **92**(4), 045414 (2015).
14. Z. Guo, X. Wu, T. Zhu, X. Zhu, L. Huang, Z. Guo, X. Wu, T. Zhu, X. Zhu, and L. Huang, "Electron-Phonon Scattering in Atomically Thin 2D Perovskites," ACS Nano **10**(11), 9992–9998 (2016).
15. S. Kumar, J. Jagielski, S. Yakunin, P. Rice, Y. C. Chiu, M. Wang, G. Nedelcu, Y. Kim, S. Lin, E. J. Santos, M. V. Kovalenko, and C. J. Shih, "Efficient Blue Electroluminescence Using Quantum-Confined Two-Dimensional Perovskites," ACS Nano **10**(10), 9720–9729 (2016).
16. G. Jia, Z. J. Shi, Y. D. Xia, Q. Wei, Y. H. Chen, G. C. Xing, and W. Huang, "Super air stable quasi-2D organic-inorganic hybrid perovskites for visible light-emitting diodes," Opt. Express **26**(2), A66–A74 (2018).
17. Z. Yang, Y. Deng, X. Zhang, S. Wang, H. Chen, S. Yang, J. Khurgin, N. X. Fang, X. Zhang, and R. Ma, "High-Performance Single-Crystalline Perovskite Thin-Film Photodetector," Adv. Mater. **30**(8), 1704333 (2018).
18. M. Saba, F. Quochi, A. Mura, G. Bongiovanni, V. Sarritzu, N. Sestu, C. Figus, M. Aresti, R. Piras, A. Geddo Lehmann, C. Cannas, A. Musinu, F. Quochi, A. Mura, and G. Bongiovanni, "Excited State Properties of Hybrid Perovskites," Acc. Chem. Res. **49**(1), 166–173 (2016).

19. V. D'Innocenzo, G. Grancini, M. J. P. Alcocer, A. R. S. Kandada, S. D. Stranks, M. M. Lee, G. Lanzani, H. J. Snaith, and A. Petrozza, "Excitons versus free charges in organo-lead tri-halide perovskites," Nat. Commun. **5**(1), 3586 (2014).
20. H. He, Q. Yu, H. Li, J. Li, J. Si, Y. Jin, N. Wang, J. Wang, J. He, X. Wang, Y. Zhang, and Z. Ye, "Exciton localization in solution-processed organolead trihalide perovskites," Nat. Commun. **7**, 10896 (2016).
21. D. Niesner, O. Schuster, M. Wilhelm, I. Levchuk, A. Osvet, S. Shrestha, M. Batentschuk, C. Brabec, and T. Fauster, "Temperature-dependent optical spectra of single-crystal $(CH_3NH_3)PbBr_3$ cleaved in ultrahigh vacuum," Phys. Rev. B **95**(7), 075207 (2017).
22. T. T. H. Do, A. G. Aguila, C. Cui, J. Xing, Z. Ning, and Q. Xiong, "Optical study on intrinsic exciton states in high-quality $CH_3NH_3PbBr_3$ single crystals," Phys. Rev. B **96**(7), 075308 (2017).
23. S. A. Veldhuis, P. P. Boix, N. Yantara, M. Li, T. C. Sum, N. Mathews, and S. G. Mhaisalkar, "Perovskite Materials for Light-Emitting Diodes and Lasers," Adv. Mater. **28**(32), 6804–6834 (2016).
24. A. R. Srimath Kandada and A. Petrozza, "Photophysics of Hybrid Lead Halide Perovskites: The Role of Microstructure," Acc. Chem. Res. **49**(3), 536–544 (2016).
25. D. W. deQuilettes, S. M. Vorpahl, S. D. Stranks, H. Nagaoka, G. E. Eperon, M. E. Ziffer, H. J. Snaith, and D. S. Ginger, "Impact of microstructure on local carrier lifetime in perovskite solar cells," Science **348**(6235), 683–686 (2015).
26. S. Colella, M. Mazzeo, A. Rizzo, G. Gigli, and A. Listorti, "The Bright Side of Perovskites," J. Phys. Chem. Lett. **7**(21), 4322–4334 (2016).
27. M. S. Alias, I. Dursun, M. I. Saidaminov, E. M. Diallo, P. Mishra, T. K. Ng, O. M. Bakr, and B. S. Ooi, "Optical constants ofCH3NH3PbBr3 perovskite thin films measured by spectroscopic ellipsometry," Opt. Express **24**(15), 16586–16594 (2016).
28. A. Poglitsch and D. Weber, "Dynamic disorder in methylammoniumtrihalogenoplumbates (II) observed by millimeter-wave spectroscopy," J. Chem. Phys. **87**(11), 6373–6378 (1987).
29. L. Dou, A. B. Wong, Y. Yu, M. Lai, N. Kornienko, S. W. Eaton, A. Fu, C. G. Bischak, J. Ma, T. Ding, N. S. Ginsberg, L. W. Wang, A. P. Alivisatos, and P. Yang, "Atomically thin two-dimensional organic-inorganic hybrid perovskites," Science **349**(6255), 1518–1521 (2015).
30. S. Ke, C. Chen, N. Fu, H. Zhou, M. Ye, P. Lin, W. Yuan, X. Zeng, L. Chen, and H. Huang, "Transparent Indium Tin Oxide Electrodes on Muscovite Mica for High-Temperature-Processed Flexible Optoelectronic Devices," ACS Appl. Mater. Interfaces **8**(42), 28406–28411 (2016).
31. M. I. Saidaminov, A. L. Abdelhady, B. Murali, E. Alarousu, V. M. Burlakov, W. Peng, I. Dursun, L. Wang, Y. He, G. Maculan, A. Goriely, T. Wu, O. F. Mohammed, and O. M. Bakr, "High-quality bulk hybrid perovskite single crystals within minutes by inverse temperature crystallization," Nat. Commun. **6**(1), 7586 (2015).
32. M. Saba, F. Quochi, A. Mura, and G. Bongiovanni, "Excited State Properties of Hybrid Perovskites," Acc. Chem. Res. **49**(1), 166–173 (2016).
33. M. J. Hollas, *Modern Spectroscopy (4th ed.)* (Wiley, 1996).
34. H. W. Yoon, D. R. Wake, and J. P. Wolfe, "Effect of exciton-carrier thermodynamics on the GaAs quantum well photoluminescence," Phys. Rev. B Condens. Matter **54**(4), 2763–2774 (1996).
35. M. Fox, *Optical Properties of Solids Oxford* (2001).
36. M. Grundmann, *The Physics of Semiconductors (2th ed.)* (Springer, 2010).
37. T. J. Savenije, C. S. Ponseca, Jr., L. Kunneman, M. Abdellah, K. Zheng, Y. Tian, Q. Zhu, S. E. Canton, I. G. Scheblykin, T. Pullerits, A. Yartsev, and V. Sundström, "Thermally activated exciton dissociation and recombination control the carrier dynamics in organometal halide perovskite," J. Phys. Chem. Lett. **5**(13), 2189–2194 (2014).
38. M. Leroux, N. Grandjean, B. Beaumont, G. Nataf, F. Semond, J. Massies, and P. Gibart, "Temperature quenching of photoluminescence intensities in undoped and doped GaN," J. Appl. Phys. **86**(7), 3721–3728 (1999).
39. T. Schmidt, K. Lischka, and W. Zulehner, "Excitation-power dependence of the near-band-edge photoluminescence of semiconductors," Phys. Rev. B Condens. Matter **45**(16), 8989–8994 (1992).
40. F. Luckert, M. V. Yakushev, C. Faugeras, A. V. Karotki, A. V. Mudryi, and R. W. Martin, "Excitation power and temperature dependence of excitons in CuInSe2," J. Appl. Phys. **111**(9), 093507 (2012).
41. J. Enderlein and R. Erdmann, "Fast fitting of multi-exponential decay curves," Opt. Commun. **134**(1-6), 371–378 (1997).
42. Y. Sun, O. Brandt, S. Cronenberg, S. Dhar, H. T. Grahn, K. H. Ploog, P. Waltereit, and J. S. Speck, "Nonpolar InxGa1-xN/GaN (1-100) multiple quantum wells grown on γ-$LiAlO_2$ (100) by plasma-assisted molecular-beam epitaxy," Phys. Rev. B Condens. Matter Mater. Phys. **67**(4), 041306 (2003).
43. T. Onuma, A. Chakraborty, B. A. Haskell, S. Keller, S. P. DenBaars, J. S. Speck, S. Nakamura, U. K. Mishra, T. Sota, and S. F. Chichibu, "Localized exciton dynamics in nonpolar (11-20) InxGa1-xN multiple quantum wells grown on GaN templates prepared by lateral epitaxial overgrowth," Appl. Phys. Lett. **86**(15), 151918 (2005).
44. X. Wen, Y. Feng, S. Huang, F. Huang, Y. B. Cheng, M. Green, and A. H. Baillie, "Defect trapping states and charge carrier recombination in organic–inorganic halide perovskites," J. Mater. Chem. C Mater. Opt. Electron. Devices **4**(4), 793–800 (2016).
45. T. Ye, X. Jiang, D. Wan, X. Wang, J. Xing, T. Venkatesan, Q. Xiong, and S. Ramakrishna, "Ultrafast Photogenerated Hole Extraction/Transport Behavior in a CH3 NH3 PbI3 /Carbon Nanocomposite and Its Application in a Metal-Electrode-Free Solar Cell," ChemPhysChem **17**(24), 4102–4109 (2016).

46. F. A. Majumder, S. Shevel, V. G. Lyssenko, H. E. Swoboda, and C. Klingshirn, “Luminescence and gain spectroscopy of disordered CdS1−xSe x under high excitation,” Z. Phys. B Con. Mat. **66**, 409–418 (1987).
47. S. Tongay, J. Suh, C. Ataca, W. Fan, A. Luce, J. S. Kang, J. Liu, C. Ko, R. Raghunathanan, J. Zhou, F. Ogletree, J. Li, J. C. Grossman, and J. Wu, “Defects activated photoluminescence in two-dimensional semiconductors: interplay between bound, charged, and free excitons,” Sci. Rep. **3**(1), 2657 (2013).
48. H. S. Duan, H. Zhou, Q. Chen, P. Sun, S. Luo, T.-B. Song, B. Bob, and Y. Yang, “The identification and characterization of defect states in hybrid organic-inorganic perovskite photovoltaics,” Phys. Chem. Chem. Phys. **17**(1), 112–116 (2015).
49. J. C. Blancon, H. Tsai, W. Nie, C. C. Stoumpos, L. Pedesseau, C. Katan, M. Kepenekian, C. M. M. Soe, K. Appavoo, M. Y. Sfeir, S. Tretiak, P. M. Ajayan, M. G. Kanatzidis, J. Even, J. J. Crochet, and A. D. Mohite, “Extremely efficient internal exciton dissociation through edge states in layered 2D perovskites,” Science **355**(6331), 1288–1292 (2017).
50. J. M. Richter, M. Abdi-Jalebi, A. Sadhanala, M. Tabachnyk, J. P. H. Rivett, L. M. Pazos-Outón, K. C. Gödel, M. Price, F. Deschler, and R. H. Friend, “Enhancing photoluminescence yields in lead halide perovskites by photon recycling and light out-coupling,” Nat. Commun. **7**, 13941 (2016).
51. Y. Fang, H. Wei, Q. Dong, and J. Huang, “Quantification of re-absorption and re-emission processes to determine photon recycling efficiency in perovskite single crystals,” Nat. Commun. **8**, 14417 (2017).